ACS APPLIED ENERGY MATERIALS

www.acsaem.org Article

Synergistic Effects of FeCo Bimetallic Single-Atom Catalysts: Accelerating the Redox Conversion of Polysulfides and Inhibiting the Growth of Lithium Dendrites in Lithium−Sulfur Batteries

Penghao Song,[‖] Surong Zheng,[‖] Zaka Ullah, Zairui Yang, Penghao Zhu, Aihua He, Cunguo Wang,* and Qi Li*

Cite This: *ACS Appl. Energy Mater.* 2023, 6, 4671−4682 Read Online

ACCESS | Metrics & More | Article Recommendations | Supporting Information

ABSTRACT: The shuttle effect of lithium polysulfides on a positive electrode and the uncontrollable growth of lithium dendrites on a negative electrode are the two fundamental crucial problems of lithium−sulfur batteries (LSBs). These problems have led to low actual specific capacity and poor rate performance of these batteries. In order to resolve these issues at both electrodes simultaneously, we used Fe and Co bimetallic atoms to dope the three-dimensional dodecahedron material ZIF-8, which is used as a monomer to construct a functional modified separator. Owing to the porous structure, high specific surface area, notable interfacial electron conductivity after carbonization, and the synergistic catalytic effect of Fe and Co bimetallic doping, the FeCoDA-CN@PP separator suppresses the shuttle effect of lithium polysulfides (LiPSs) on the positive electrode and ensures the higher ion/electron rapid diffusion and hence efficient lithium growth during the cycling on the negative electrode. The demonstrated LSBs with the FeCoDA-CN@PP separator deliver a specific discharge capacity of 1404 mAh g^{-1} at 0.1C. After 500 provided cycles at a rate of 1C, it still offers a specific discharge capacity of 541 mAh g^{-1} and a stable Coulombic efficiency of >98% with a capacity decay rate of 0.08% per cycle. At a discharge rate of 1 mA cm^{-2}, the symmetrical battery with the FeCoDA-CN@PP separator was still able to maintain a stable voltage distribution and an overpotential of 31 mV after 500 h. The outcomes pave an auspicious approach for the development of LSBs with long-cycle life and higher capacity, which may further promote the industrialization and commercialization of LSBs.

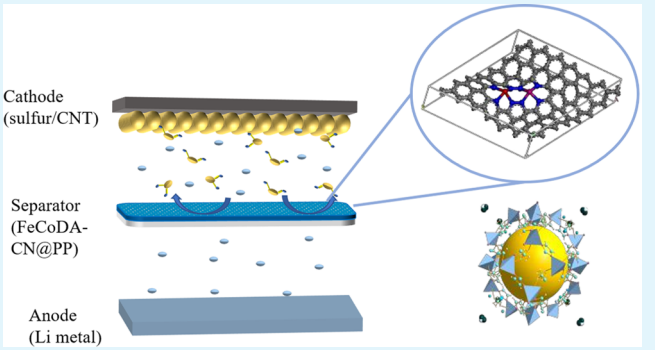

KEYWORDS: *lithium−sulfur battery, separator modification, shuttle effect, double single-atom catalysts, electrocatalysts, kinetics*

1. INTRODUCTION

The swift developments of modern technologies are demanding significant research attention to assemble advanced energy storage materials.[1] Whether these are portable electronic devices, electric vehicles, or hybrid machines, energy storage materials are needed to assemble the devices like lithium−sulfur batteries (LSBs) to fulfill their needs. LSBs require low-cost sulfur raw materials, deliver higher theoretical specific capacity up to 1675 mAh g^{-1}, offer markable energy density up to 2600 Wh kg^{-1}, and produce lower environmental pollution.[2−4] Owing to these properties, a sulfur cathode is included in next-generation cathode materials for propitious developments. However, the commercialization journey of LSBs is not so smooth. There are some serious concerns that strongly need to be addressed.[5] For instance, the volume expansion effect of S in the sulfur cathode, formation of Li_2S insulation (dead sulfur), rapid capacity decay, and the shuttle effect of polysulfide, which reduces the Coulombic efficiency of the battery. Moreover, there is growth of lithium dendrites on the lithium metal cathode surface; it is produced after a certain number of cycles owing to the uneven coating of lithium, which is also an inevitable problem.[6−8]

Researchers are making continuous efforts to maximize the performance of LSBs, particularly through designing and modification of cathodes, anodes, separators, and intervening interlayers. For instance, researchers are working on the assembly of highly conductive and porous carbon nanomaterials with large surface areas, which improves the efficiency of sulfur loading,[9,10] addition of ionic groups to the electrode material, which encourages the uniform deposition of lithium ions in the electrolyte,[11−15] and modification of traditional

Received: January 3, 2023
Accepted: April 19, 2023
Published: April 27, 2023

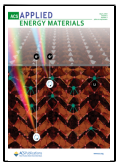

https://doi.org/10.1021/acsaem.2c04118
ACS Appl. Energy Mater. 2023, 6, 4671−4682

separators, which boosts the performance of the battery.[16,17] However, most of the conducted research addresses only one problem of a specific type of battery at one time.[18−20] To put the LSBs on commercialization as soon as possible, researchers should focus on solving the multiple problems of cathode and anode at the same time.

The separator is placed in the battery between the cathode and the anode. It is an important bridge that indirectly connects the cathode with the anode and prevents direct contact between them. It is a crucial factor to ensure the safety of the battery.[21−24] Therefore, a reasonable design or modification of the LSB separator not only solves the problem of the sulfur cathode but also causes the lithium metal anode to reduce the generation of lithium dendrites to further increase the Li-ion flux. Since modification of the separator does not influence the contents of sulfur in the cathode, a wide variety of materials, from initial carbon materials (like graphene oxide, carbon nanotubes, and porous carbon) to later polar materials (like metal−organic frameworks and transition metal compounds), have been employed to design the separators for LSBs, which have produced some inspiring and auspicious results.[25−27]

Metal−organic frameworks (MOFs) are a popular group of polymeric coordination polymers composed of metal nodes and organic linkers with tunable geometry, controllable porosity, significant surface area, and thoroughly distributed active sites. These features suggest that the MOF-based metallic material can be more flexible for designing and preparation of bimetallic and polymetallic materials to assemble effectual catalysts with higher polysulfide ion catalysis and greater lithium-ion mobility.[28] During the last few years, several reports have been published on investigation of adsorption or catalysis of polysulfides using monometallic atomic MOFs. For instance, a study shows that the use of open Ce−MOF atoms as catalytic centers can rapidly adsorb polysulfide ions into the pore channels owing to its thoroughly dispersed catalytic sites and larger specific surface; thus, the proposed scheme facilitates the catalytic conversion of metal nodes to short-chain polysulfides.[29] However, single adsorption cannot reduce the shuttle effect efficiently owing to the limited adsorption capability of single metal atoms at active sites.[30]

When soluble lithium polysulfides (LiPSs) could not rapidly be converted into insoluble short-chain polysulfides (which are then redeposited on the cathode), the active sites on the separator become occupied. This situation leads to a loss in the active material, and the modified layer becomes less effective. Contrary to this, when adsorption of the material on LiPSs is lower, LiPSs could not develop effective contact with catalytic sites to enhance the catalytic impact of the material. Therefore, it is necessary to further modulate the MOFs (like introduction of defects and adjustment of metal centers) to balance the synergistic influence of catalysis and adsorption. The bimetallic single-atom MOFs contain two sets of monoatomic structures: flexible bimetallic sites, which provide more possibilities to tune the geometrical configurations, and an electronic structure, which provides more opportunities to adjust the binding strength of reaction intermediates and optimization of catalytic activity/selectivity. Moreover, the double-atom catalysts (DACs) can perform their different functions during the reactions and enhance atomic utilization. It is worth mentioning that the bimetallic single-atom MOFs simultaneously increase the diffusion rate of lithium ions, encourage their uniform deposition on the surface of the lithium metal anode, and inhibit the nucleation and growth of lithium metal anode dendrites.[31−33]

Herein, we present the assembly of a nitrogen-rich porous carbon material modified with MOF-derived bimetallic single atoms (FeCoDA-CN). The MOFs with ZIF-8 as a key material retain their original shape after carbonization. The regular dodecahedral morphology and its three-dimensional structure provide multiple attachment sites to Fe and Co single atoms to boost the polysulfide conversion, and the porous structure of MOFs ensures the high Li^+ flux after carbonization. The FeCoDA-CN@PP bifunctional membrane is designed and fabricated by modifying the polypropylene (PP) surface with poly(vinylidene fluoride) (PVDF) as a binder, which not only encourages high Li^+ flux but also accelerates the polysulfide reaction kinetics through the synergistic catalysis of bimetallic atoms as well as inhibits the shuttling of LiPS. The LSBs assembled with the FeCoDA-CN@PP separator could reach a higher initial capacity of ≈1404 mAh g^{-1} at 0.1C. Even at a higher rate of 2C, the capacity still shows a higher value of ≈652 mAh g^{-1} and outstanding cycle stability for 500 cycles with a decay rate of 0.08% per cycle (at 1C). The exceptional electrochemical response of the optimized FeCoDA-CN@PP separator offers a fruitful approach for the commercial preparation of suitable separators for future LSBs.

2. MATERIALS AND METHODS

2.1. Materials. All chemicals were of analytical grade and no pretreatment was employed before use. 2-Methylimidazole, $Zn(NO_3)_2{\cdot}6H_2O$, $Co(NO_3)_2{\cdot}6H_2O$, iron acetylacetonate ($Fe(acac)_3$), *N*-methyl-pyrrolidone (NMP), anhydrous ethanol (EtOH), methanol, and *N*,*N*-dimethylformamide (DMF) were purchased from Sinopharm, China. Sulfur, multiwalled carbon nanotubes, and polypropylene (PP) separator were, respectively, purchased from Shanghai Aladdin Pharmaceuticals (China), Nanjing XFNANO (China), and Celgard (USA), whereas LiTFSI in DOL/DME (v/v = 1:1 +2% $LiNO_3$) and lithium tablets were purchased from Nanjing Moges Energy Technology, China.

2.2. Synthesis of Fe-ZIF-8, Co-ZIF-8, and FeCo-ZIF-8. 4.41 g of 2-methylimidazole was dissolved in 90 mL of methanol. Another 90 mL of methanol was dissolved in 0.353 mg of $Fe(acac)_3$ and 3.27 g of $Zn(NO_3)_2{\cdot}6H_2O$. The rest of the procedure was similar to that of the synthesis of 2-methylimidazole zinc salt (ZIF-8).[34] Moreover, Fe-ZIF-8 can also be prepared following a similar procedure. Also, the preparation of Co-ZIF-8 was very similar to that of Fe-ZIF-8, except that 293 mg of $Co(NO_3)_2{\cdot}6H_2O$ was added to the anhydrous methanol solution. In the synthesis of FeCo-ZIF-8, 176 mg of $Fe(acac)_3$ and 147 mg of $Co(NO_3)_2{\cdot}6H_2O$ were added to the solution, and the ratio of 2-methylimidazole and $Zn(NO3)_2{\cdot}6H_2O$ was kept same as that of before.

2.3. Preparation of FeCoDA-CN, CoSA-CN, and FeSA-CN. For the preparation of FeCoDA-CN, dried FeCo-ZIF-8 was transferred to a tube furnace. The temperature of the sample was increased at a rate of 5 °C min^{-1} to 950 °C and its annealing was performed at this temperature in an Ar atmosphere (100 sccm) for 3 h. After the furnace was cooled to room temperature, the final product in the form of powder was obtained, which was named FeCoDA-CN. For comparison, CoSA-CN and FeSA-CN were also prepared through a similar method by respectively using Co-ZIF-8 and Fe-ZIF-8 as precursors.

2.4. Preparation of FeCoDA-CN@PP, CoSA-CN@PP, and FeSA-CN@PP. The as-synthesized FeCoDA-CN and poly(vinylidene fluoride) (PVDF) (mass ratio 4:1) were dispersed in NMP and their stirring was performed for 12 h. Later, the obtained slurry was coated on the PP membrane using the doctor blade to get the separator, FeCoDA-CN@PP. The dried separator was shaped into a wafer of 19 mm diameter, where the average loading mass was determined as 1.56

https://doi.org/10.1021/acsaem.2c04118
ACS Appl. Energy Mater. 2023, 6, 4671−4682

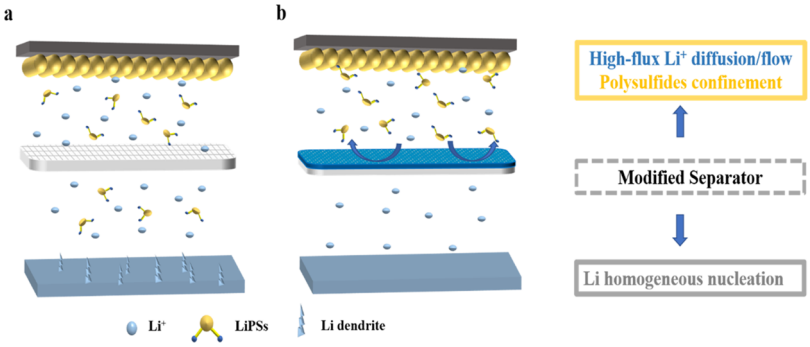

Figure 1. Schematic diagram illustrating the working mechanism of LSBs with PP (a) and FeCoDA-CN@PP separator (b).

mg cm^{-2}. For comparative analysis, the CoSA-CN- and FeSA-CN-modified separators (respectively CoSA-CN@PP and FeSA-CN@PP) were also prepared using a similar process. The CoSA-CN@PP and FeSA-CN@PP interlayer loading was optimized and a medium loading of 1.56 mg cm^{-2} was employed.

2.5. Synthesis of Li_2S_4 Solution and Adoption Tests. For the preparation of the Li_2S_4 solution, the procedure was followed as reported in the literature.[28] In short, S and Li_2S with a molar ratio of 3:1 were dissolved in a 1,3-dioxolane/1,2-dimethoxyethane solution (DOL/DME, volume ratio was 1:1), and stirring of the solution was performed overnight. After the chemical reaction took place, a homogeneous Li_2S_4 solution was obtained. 60 mg of FeSA-CN, CoSA-CN, and FeCoDA-CN were added to the Li_2S_4 solution in an Ar atmosphere to evaluate the polysulfide absorption ability of these materials.

2.6. Material Characterization. A scanning electron microscope (SEM, HITACHI S-4800, Japan) was engaged to examine the morphological features of the prepared samples, and a field emission transmission electron microscope (Tecnai G2 F20 S-Twin) was employed to investigate the porous structure of the samples and their elemental distributions, whereas a Titan Cubed Themis G2-300 aberration-corrected scanning transmission electron microscope (AC-STEM) was used to further characterize the FeCoDA-CN. For the determination of the crystal structures of the prepared samples, an X-ray diffractometer (Thermo Fisher ESCALAB 250Xi) was employed to study the X-ray diffraction response. Inductively coupled plasma atomic emission spectroscopy (Perkin Elmer) was performed to determine the loading of iron on the sample. The Brunauer–Emmett–Teller (BET) results were obtained using a surface area and pore size analyzer (TriStar II 3020, Micromeritics Instrument Co.) to study the specific surface area and pore size distribution, whereas a thermogravimetric analysis (TGA) appliance (Q5000, TA Instruments) was used to determine the contents of sulfur in the prepared samples. X-ray photoelectron spectroscopy (XPS) was performed on a PHI instrument (PHI 5000 Versa Probe, Ulvac-Phi, Japan) using monochromatic Al Kα radiation (225 W, 15 mA, 15 kV) to study the chemical characteristics of FeCoDA-CN. A Shirley-type background subtraction approach was adopted for the curve fitting of XPS spectra. A Raman spectrometer (LabRam HR800-UV-NIR, HORIBA Jobin Yvon, Paris, France) with an excitation laser of wavelength 532 nm was used to record the Raman spectra. Moreover, a microcomputer-controlled universal material testing machine (Instron 3365, Instron) was used to examine the longitudinal tensile strength of the prepared samples.

2.7. Electrochemical Characterization. For electrochemical measurements, CNTs and sulfur (with mass ratio 3:7) were mixed together, kept at 155 °C for 12 h to make sulfur evenly penetrate into the CNTs, and then cooled to room temperature to obtain CNTs/S composites. About 80 wt % CNTs/S composite, 10 wt % carbon black, and 10 wt % PVDF binder were mixed together in *N*-methyl-2-pyrrolidone (NMP) solvent to get the positive electrode slurry. The homogenous slurry was then applied on aluminum foil with a spatula. It was dried in vacuum at 60 °C. Later, it was shaped into small discs with a diameter of 13 mm. The areal loading of sulfur in the electrode was around 2.5 mg cm^{-2}. These discs were used as positive electrodes for lithium metal batteries. A CR2025 button battery and a Li–Li symmetrical cell were assembled inside an Ar-filled glovebox. The CR2025 button battery was fabricated by sandwiching the modified PP separators between metal lithium sheets. For this, 1 M LiTFSI in DOL/DME (v/v, 1:1) with a 2.0 wt % $LiNO_3$ additive was used as an electrolyte (~0.6 μL). The cyclic voltammetry (CV) measurements and rate capacity tests were performed for the applied voltage range of 1.7–2.8 V on a Chi760e electrochemical workstation, whereas the cycle stability was tested for a voltage range of 1.7–2.8 V using a Neware Battery Testing System. The lithium-ion transference number (t_{Li^+}) was determined using the following relation

$$t_{Li^+} = \frac{I_{ss}(\Delta V - I_o R_o)}{I_o(\Delta V - I_{ss} R_{ss})} \quad (1)$$

where I_{ss}, I_o, R_{ss}, and R_o, respectively, represent the steady-state current, initial-state current, steady-state resistance, and initial-state resistance. Also, ΔV represents the steady-state voltage subtracted from the initial-state voltage, which was considered as 10 mV.

2.8. Theoretical Calculations. Density functional theory (DFT) was employed to investigate the catalytic mechanism of FeCoDA. In this study, the computational simulation module CASTEP and the generalized functions GGA and PBE were used. The cutoff energy was fixed as 400 eV and the *k*-point was determined as 3 × 3 × 1. The pressure tolerance, force tolerance, energy tolerance, and maximum displacement were set, respectively, as 0.2 GPa, 0.1 eV $Å^{-1}$, 5.0 × 10^{-5} eV/atom, and 0.005 Å, and the maximum number of iterations was set to 100. In addition, the self-consistent field (SCF) tolerance and the maximum SCF cycle were customized as 1.0 × 10^{-5} eV/atom and 1000, respectively. The following equation was used for Li_2S adsorption energy measurement

$$E_{ab} = E_{total} - E_{sub} - nE_{Li_2S} \quad (2)$$

where E_{total} represents the total energy possessed by the system after adsorption of Li_2S, E_{sub} denotes the total energy of the substrate, and E_{Li_2S} gives the energy of a single Li_2S molecule.

3. RESULTS AND DISCUSSION

A separator is an influential part of the battery, as illustrated in Figure 1. In LSBs, a conventional PP separator separates the two electrodes to avoid the contact while ensuring Li^+ migration forth and back between the two electrodes. However, a conventional PP separator cannot prevent the polysulfides from shuttling between the anode and the cathode. Soluble polysulfides move to the anode and produce insoluble Li_2S on the lithium metal surface, which leads to a significant decrease in sulfur utilization and rapid capacity degradation. Moreover, the growth of lithium dendrites on the negative electrode cannot effectively be suppressed due to increased polarization caused by passivation of the lithium metal. More active surfaces are exposed during the uneven

https://doi.org/10.1021/acsaem.2c04118
ACS Appl. Energy Mater. 2023, 6, 4671–4682

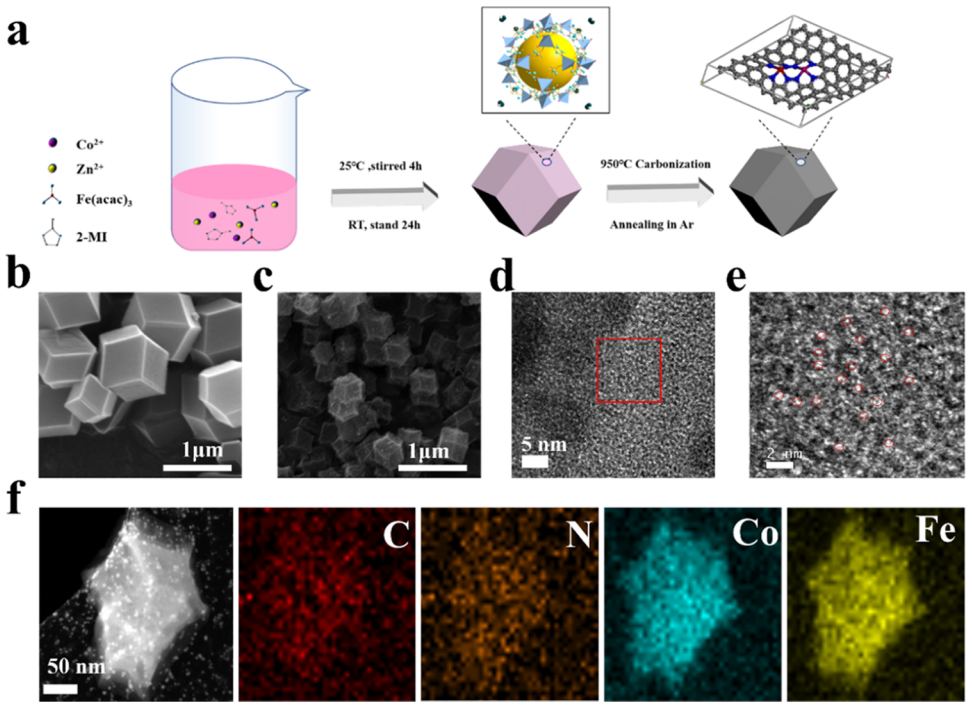

Figure 2. Preparation route and morphological analysis. (a) Schematic diagram depicting the synthesis procedure of FeCoDA-CN assembly. SEM micrographs of (b) FeCo-ZIF-8 and (c) FeCoDA-CN. (d, e) HADDF-STEM views of FeCoDA-CN. (f) EELS mapping for C, N, Co, and Fe in FeCoDA-CN, demonstrating the homogeneous distribution of single Fe and Co atoms in FeCoDA-CN.

lithium plating and stripping process, which leads to an increase in the contact area of lithium with the electrolyte and an increase in electrolyte consumption. This situation greatly increases the internal resistance of the cell.

In this work, an FeCo diatomic-modified nitrogen-rich material is introduced and coated on a PP separator, which lies between the positive and negative electrodes. On the positive electrode, the catalytic effect is enhanced, and strong adsorption of FeCoDA-CN on LiPSs prevents the diffusion of polysulfides to the negative electrode through the separator. Moreover, the standard dodecahedral structure of FeCoDA-CN sustains after carbonization, which ensures the high flux migration of lithium ions. The substantial specific surface area provides abundant attachment sites for LiPSs. In addition, the inherent metallic properties of MOFs doped with metal atoms can reduce the interfacial resistance of the separator and the electrode and assists in achieving lower polarization as well as faster sulfur conversion kinetics, whereas on the negative electrode, FeCoDA-CN offers a high ionic conductivity, and its relatively uniform stacked structure ensures the uniform deposition of lithium ions at the negative electrode and separator interface to restrict the growth of lithium dendrites. In this scenario, the FeCoDA-CN-modified PP separator can remarkably advance the efficiency of LSBs.

The route for FeCoDA-CN synthesis is shown in Figure 2a. The synthesis of FeSA-CN and CoSA-CN is also carried out using the same route. This approach assembles the materials having dodecahedron structures with uniform size and shape (Figures 2b and S1a,b,d,e). The morphology of these materials is similar to that of ZIF-8. The basic dodecahedral morphology (Figures 2c and S1c,f) is also maintained after the carbonization at 950 °C for 3 h in an Ar atmosphere. However, a slight shrinkage is induced in the material, which is attributed to the loading modification of Fe and Co atoms.

The high-resolution TEM image of FeCoDA-CN does not show any obvious metal nanoparticles on its surface (Figure 2d). Instead, there are massive micropores on the FeCoDA-CN surface, which confirm its porous structure and evidence the doping of Fe and Co in CN at the atomic level. Furthermore, the high-angle annular dark field scanning transmission electron microscopy (HAADF-STEM) view at atomic resolution given in Figure 2e shows bright spots, which correspond to atomic pairs. Quantitative analysis by line scan on the contrast of the HAADF-STEM image across the atom pair (Figure S2) reveals that the distance between the two peaks is 0.23 nm, illustrating that the adjacent metal atoms form double-atom sites instead of discrete single-atom sites. These bright spots are uniformly distributed with a size of ∼1 Å, which confirms the presence of single metal atoms. Besides, Figure 2f shows the homogeneous distribution of Fe and Co species in FeCoDA-CN as revealed by electron energy-loss spectroscopy (EELS) analysis.

The PP separator is coated with an atomically doped carbon material and is reshaped into wafers with a diameter of 19 mm through a punching approach (Figure S3a). Also, FeCoDA-CN after carbonization is coated on the PP separator (Figure S3b), where the thickness of the modified coating is ∼15 μm (1.56 mg cm^{-2}), as given in Figure S3d. And the catalyst uniformly coated on the PP separator still maintains a regular polyhedral structure (Figure S3), which facilitates the transport of lithium ions. The vacuum-dried separator remains unbroken after multiple bending tests, which reflects its good mechanical strength and flexibility (Figure S5a−d). Figure S6 shows the wetting performance of PP and FeCoDA-CN@PP separators on the electrolyte, where the latter has a good wetting performance with a contact angle of 11.2 on the electrolyte. Figure S7 shows the stress−strain curves of four separators, which determine the modulus of FeSA-CN@PP (615.96

https://doi.org/10.1021/acsaem.2c04118
ACS Appl. Energy Mater. 2023, 6, 4671−4682

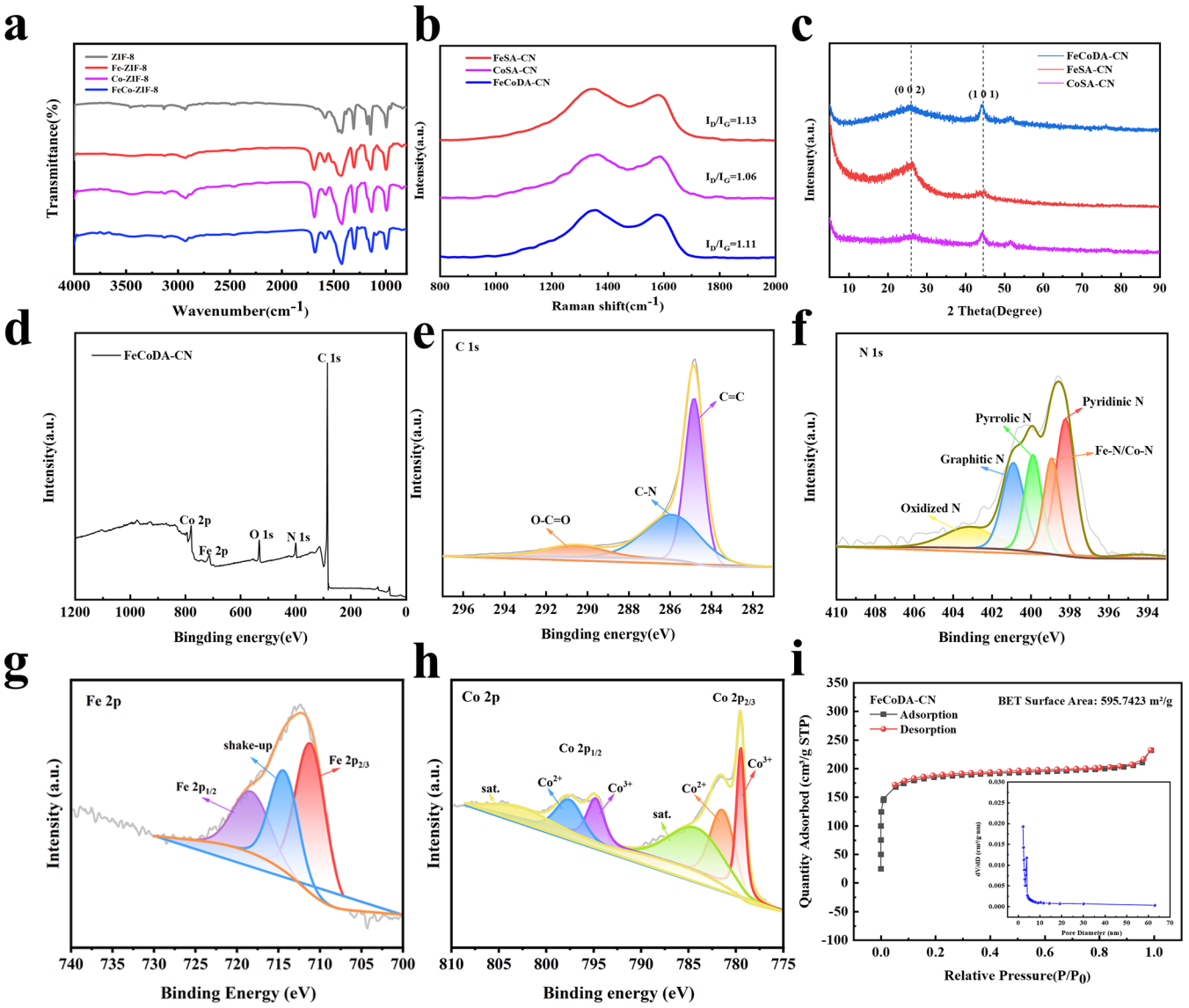

Figure 3. Structural analysis of the FeCoDA-CN composite. (a) FTIR spectra of ZIF-8, Fe-ZIF-8, Co-ZIF-8, and FeCo-ZIF-8 (b) Raman spectra and (c) XRD patterns of FeCoDA-CN, CoSA-CN, and FeSA-CN. (d) XPS of FeCoDA-CN. High-resolution XPS spectra of (e) C 1s, (f) N 1s, (g) Fe 2p, and (h) Co 2p for FeCoDA-CN. (i) Nitrogen adsorption−desorption isotherms and pore size distribution of FeCoDA-CN.

MPa), CoSA-CN@PP (634.90 MPa), and FeCoDA-CN@PP (640.74 MPa). These values are lower than that of the modulus of the PP separator (853.80 MPa). The decrease in the modulus of FeCoDA-CN@PP is valuable and meets the requirements of LSBs.

Figure 3a shows the Fourier transform infrared (FTIR) spectra of ZIF-8, Fe-ZIF-8, Co-ZIF-8, and FeCo-ZIF-8 before carbonization. The characteristic peaks at 990 and 1145 cm^{-1} indicate the stretching vibrations of C−N, whereas the absorption peaks at ∼1580 cm^{-1} are due to the stretching vibrations of the −CN group. The small peaks at 2933 and 3138 cm^{-1} are the absorption peaks for the C−H bond and the methyl group on the imidazole ring, respectively. The presence of basic characteristic peaks of ZIF-8 confirms the successful synthesis of ZIF-8 materials with different metal atom doping and diatomic codoping. Raman spectra given in Figure 3b show the broader *D* and *G* peaks at 1345 and 1588 cm^{-1}, respectively. The analysis shows the I_D/I_G values of FeCoDA-CN, FeSA-CN, and CoSA-CN, respectively, as 1.11, 1.13, and 1.06, which strongly suggest the low graphitization degree of carbon. It confirms the disordered carbon structure inside the material and hence suggests the hollow and porous structure of the prepared materials. Moreover, X-ray diffraction (XRD) patterns of FeCoDA-CN, FeSA-CN, and CoSA-CN given in Figure 3c show two diffraction peaks (002) and (101) for 2θ values of ∼26 and ∼44°, respectively. These results also confirm the presence of graphitic carbon with a low graphitization degree. The XRD outcomes are consistent with Raman spectroscopy results and confirm the successful synthesis of porous carbon materials.

Figure 3d shows the XPS spectrum of FeCoDA-CN and suggests that the carbonized material is doped with Fe and Co. The contents of Fe and Co are recorded, respectively, as 0.77 and 1.49% during the elemental analysis. Figures S8a and S9a support these outcomes and confirm that the single atoms were successfully doped into the prepared material with 1.12% Fe in FeSA-CN and 2.03% Co in CoSA-CN. There is also a peak for Zn, as its boiling point is 906 °C, and sometimes it could not be removed completely from the material during the carbonization at 950 °C. The high-resolution C 1s spectrum of

https://doi.org/10.1021/acsaem.2c04118
ACS Appl. Energy Mater. 2023, 6, 4671−4682

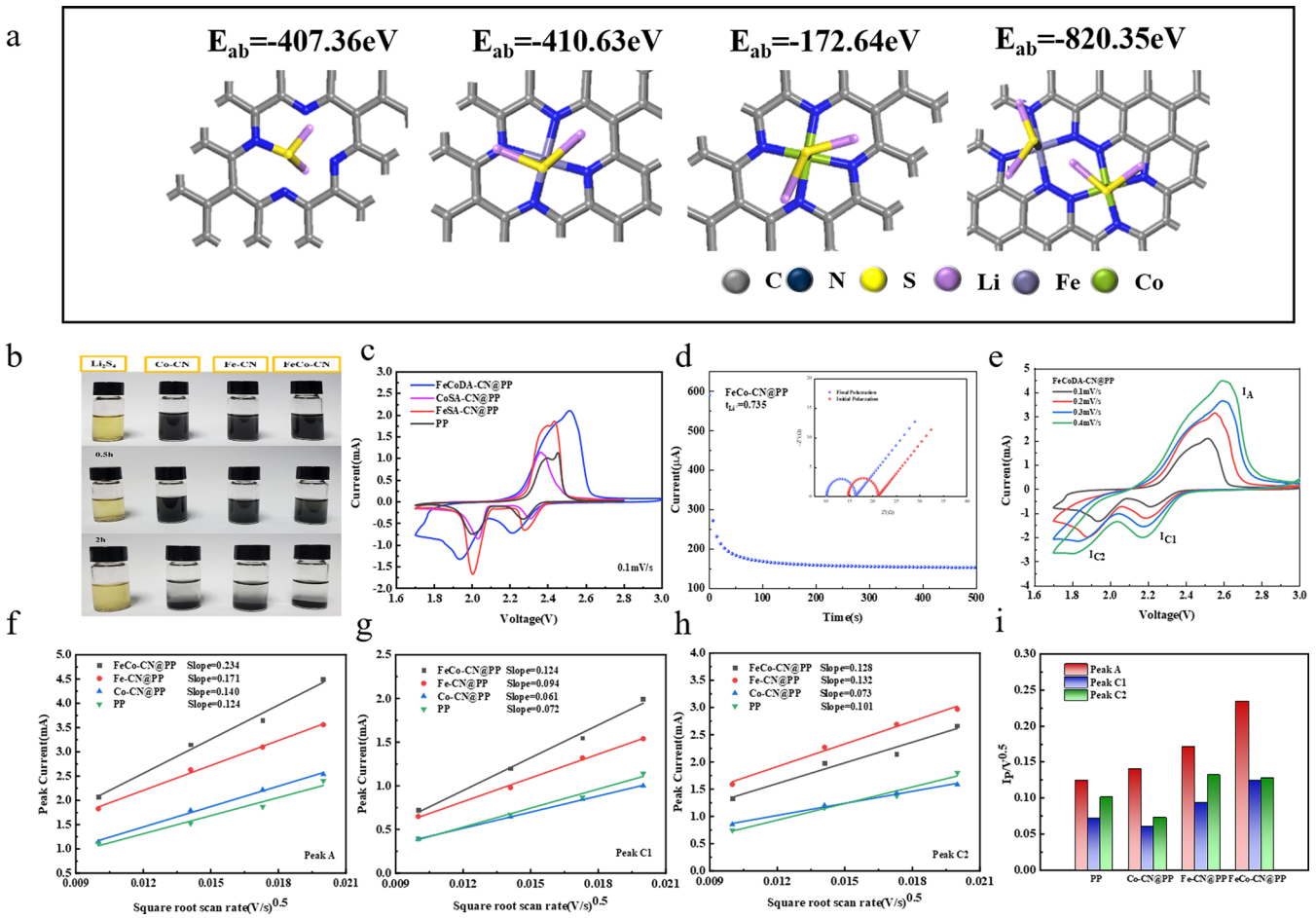

Figure 4. Electrochemical valuation of prepared materials. (a) DFT calculation models for CN@Li_2S, FeSA-CN@Li_2S, CoSA-CN@Li_2S, and FeCoDA-CN@Li_2S. (b) Photographs showing the diffusion capability of Li_2S_4 with FeSA-CN, CoSA-CN, and FeCoDA-CN. (c) CV curves of LSBs with FeCoDA-CN@PP, FeSA-CN@PP, CoSA-CN@PP, and PP separator measured at 0.1 mV s^{-1}. (d) Lithium-ion transference number of the FeCoDA-CN@PP separator determined using the Li−Li symmetrical cells. (e) CV curves of the FeCoDA-CN@PP separator recorded at varying scan rates for a potential range of 1.7−2.8 V (vs Li/Li^+). CV peak current during (f) anodic oxidation reaction (I_A), (g) first cathodic reduction reaction (I_{C1}), and (h) second cathodic reduction reaction (I_{C2}) against the square root of the scan rate. (i) Comparison of CV peak current (I_p) for different prepared separators.

FeCoDA-CN given in Figure 3e shows the peaks at 284.4, 285.2, and 288.5 eV, which are, respectively, associated with C═C, C−N, and O−C═O bonds. Figure 3f shows the high-resolution N 1s spectrum of diatomically doped FeCoDA-CN with four characteristic peaks for N atoms, which mainly exist in the form of pyridine nitrogen (398.5 eV), pyrrole nitrogen (399.8 eV), graphite nitrogen (400.8 eV), and nitrogen oxide (402.8 eV).

High-resolution Fe 2p spectra given in Figure 3g show the peaks at 712.2 and 718.4 eV, which are credited to Fe $2p_{3/2}$ and Fe $2p_{1/2}$, respectively. The satellite peak at 715.6 eV indicates the presence of Fe in FeCoDA-CN. Figures S8b,c and S9,c show the high-resolution C 1s and N 1s spectra for both FeSA-CN and CoSA-CN, whereas Figure S8d confirms the presence of Fe in FeSA-CN. Also, Figures 3h and S9d show the XPS spectra for FeCoDA-CN and CoSA-CN; these spectra show the Co 2p region with peaks for Co $2p_{3/2}$ at 778.3 eV and Co $2p_{1/2}$ at 795.9 eV. Moreover, the satellite peaks are found at 786.8 and 803.5 eV, respectively, for Co $2p_{3/2}$ and Co $2p_{1/2}$, confirming the successful doping of Co in these materials. These results demonstrate that the prepared atomically doped nitrogen-rich porous carbon materials possess notable physicochemical properties desired for the efficient electrochemical response of the material.

BET analysis is conducted to accurately determine the specific surface area of the atomically doped electrode material (Figure 3i). The I-type isotherm similar to the Langmuir adsorption isotherm suggests the mesoporous structure of the material. The specific surface area and pore volume of FeCoDA-CN are measured as 595.74 m^2 g^{-1} and 0.359 cm^3 g^{-1}, respectively. The results show that most of the pores are micropores with an average pore diameter of 8.49 nm. For FeSA-CN and CoSA-CN, the specific surface areas are measured as 595.90 and 543.71 m^2 g^{-1}, the pore volumes are recorded as 0.445 and 0.401 cm^3 g^{-1}, and the average pore diameters are found to be 5.58 and 6.96 nm, respectively (Figure S10a,b). As compared to Li^+ (~1.52 Å), the observed pore size is sufficient for lithium ions to pass through the modified separator. The relatively large pore volume and specific surface area of sulfur cathode provide conditions for the conversion and adsorption of polysulfides (~7.9 Å), as more adsorption sites will inhibit the shuttle effect.

The XPS study shows that FeCoDA is bonded to eight nitrogen atoms in a nitrogen-rich carbon matrix. Based on the obtained results, two different nitrogen-rich carbon models are

https://doi.org/10.1021/acsaem.2c04118
ACS Appl. Energy Mater. 2023, 6, 4671−4682

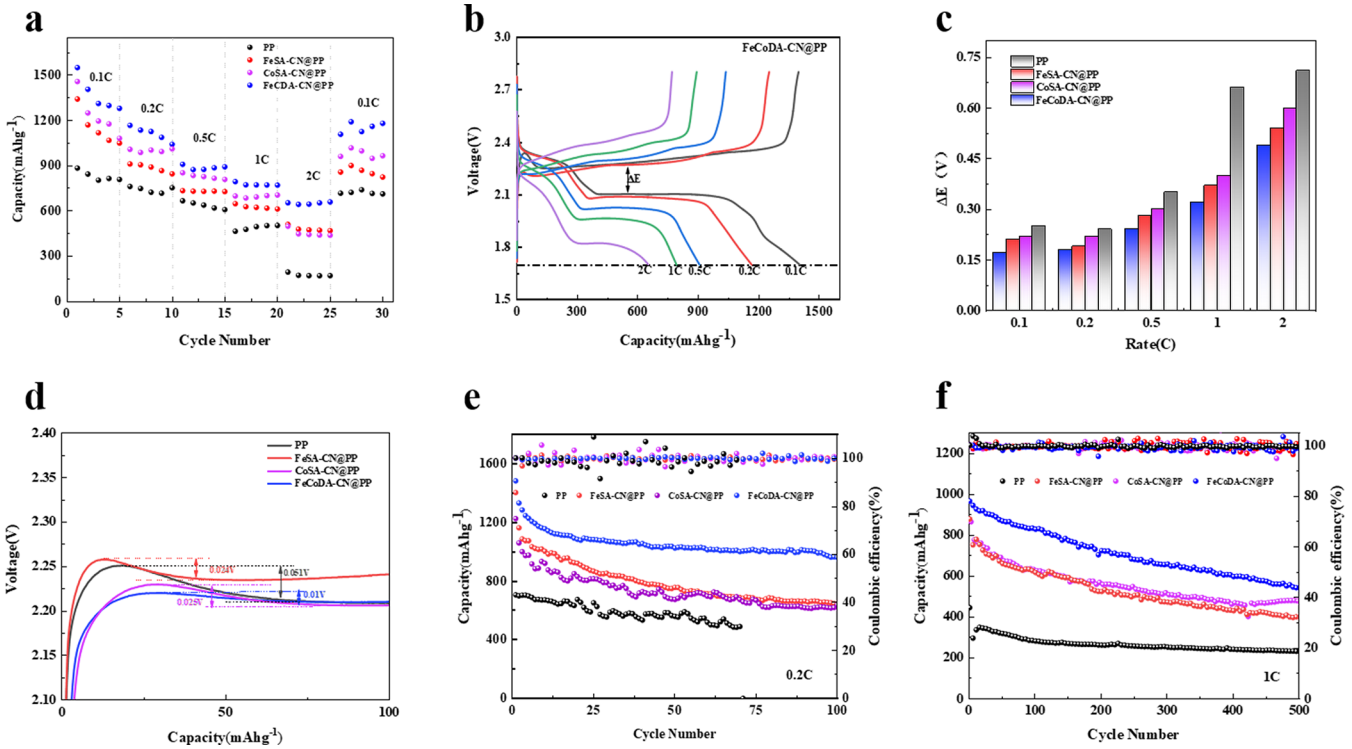

Figure 5. Evaluation of the electrochemical response of prepared materials. (a) Rate response of four different separators measured at 0.1−2C. (b) Charge profiles at the initial stage. (c) Charge/discharge curves of LSB with the FeCoDA-CN@PP separator at various rates. (d) Overpotential between the charge and discharge plateaus of LSBs with different separators measured at varying rates. Long-term cycling response of LSBs with four different separators recorded at (e) 0.2C and (f) 1C.

designed for DFT calculations (Figure 4a). By simulating the adsorption of Li_2S, the energy of each part is calculated, and adsorption energy is measured by substituting the values in eq 2. Table S1 shows that the adsorption energy of FeCoDA-CN for Li_2S (−820.35 eV) is larger than those of FeSA-CN (−410.63 eV), CoSA-CN (−172.64 eV), and CN (−407.36 eV). The smaller adsorption energy of CoSA-CN for Li_2S may be due to the larger substrate energy of CoSA-CN. In FeCoDA, the catalytic sites can increase the adsorption energy for Li_2S in two ways. First, the positively charged centers FeSA and CoSA in FeCo-N_8 can couple with negatively charged S^{x-} of LiPSs. In this way, the binding energy of Li^+ to S^{x-} is greatly reduced. Second, the positively charged centers FeSA and CoSA have a repulsive effect on Li^+ of LiPSs complexes, due to which the Li ions are easily separated from LiPSs. This situation accelerates the charging and discharging process. These outcomes are consistent with the adsorption observations (Figure 4b).

The adsorption capacity of polysulfides on the sulfur cathode is effective in promoting the polysulfide conversion kinetics and improving the cycling stability of LSBs. For results given in Figure 4b, about 60 mg each of FeCoDA-CN, FeSA-CN, and CoSA-CN are added to 6 mL of a Li_2S_4 DOL/DME (1:1) solution separately; these are mixed thoroughly with the solutions and left to stand for 0.5 and 2 h. The solutions containing FeCoDA-CN materials fade quickly and become completely colorless after 2 h, whereas FeSA -CN and CoSA-CN remain light yellow after 2 h. This indicates that FeCoDA-CN has a strong adsorption ability for lithium polysulfides. The synergistic effect of iron and cobalt atoms makes it more helpful to interact with polysulfides than single atoms. Meanwhile, to investigate the electrocatalytic ability of three atom-doped carbon materials for polysulfide conversion, the CV profiles of cells comprising PP, FeSA-CN@PP, CoSA-CN@PP, and FeCoDA-CN@PP separators are recorded at a scan rate of 0.1 mV s^{-1}, as shown in Figure 4c. The FeCoDA-CN@PP separator-based cell has the largest CV closure area, which indicates its highest actual charge/discharge specific capacity. Moreover, it has the largest oxidation current response density and higher reduction current response density, which indicates that the two-atom synergistic catalytic sites of the FeCoDA-CN material can significantly improve the polysulfide conversion kinetics. The CV curves of the Li||Li symmetric cell (Figure S12) show that FeSA-CN accelerates the conversion to soluble polysulfide by proper adsorption, CoSA-CN promotes the conversion of polysulfide to lithium sulfide by catalysis, and FeCoDA-CN promotes both phases simultaneously, which is also consistent with the literature.[34]

In order to estimate the electrochemical response of the prepared separators for LSBs, the separators are integrated into Li||Li symmetric cells, and their lithium-ion transfer rate tests are performed for original PP and modified PP separators. The Bruce Vincent equation is used to measure the migration number of Li^+ (t_{Li^+}; Figure 4d). The polarization voltage is determined as 10 mV. The resistance and instantaneous current of the initial and steady states are measured. The t_{Li^+} values for unmodified PP, FeCoDA-CN@PP, FeSA-CN@PP, and CoSA-CN@PP separators were 0.77, 0.74, 0.60, and 0.59, respectively (Figure S13a,b). These results indicate that the diatomically modified nitrogen-rich carbon material is highly efficient for the conduction and transmission of lithium ions.

CV and EIS analyses of different modified separators are performed to further evaluate the lithium-ion transfer rate. CV profiles of cells assembled with different separators show the

https://doi.org/10.1021/acsaem.2c04118
ACS Appl. Energy Mater. 2023, 6, 4671−4682

notable electrocatalytic ability of three atom-doped carbon materials for polysulfide conversion, as shown in Figures 4e and S14a−c. Cells assembled with PP separators have two strong cathodic peaks at 1.9−2.1 and 2.1−2.3 V, which are due to the reduction of sulfur to Li_2S_x ($S_8 \rightarrow Li_2S_x$) and formation of solid lithium sulfide ($Li_2S_x \rightarrow Li_2S_2/Li_2S$). In addition, the peak for anodic oxidation of the cell at 2.4−2.6 V is ascribed to reversible transformation of lithium sulfide to sulfur ($Li_2S_2/Li_2S \rightarrow S_8$). The FeCoDA-CN@PP separator has the highest peak current compared to those of FeSA-CN@PP, CoSA-CN@PP, and PP separators.

The diffusion efficiency of lithium ions (D_{Li^+}) estimates the catalytic response to boost the redox reaction of LiPSs, and rapid diffusion of lithium ions encourages sulfur conversion at the catalyst interface. The CV analysis is helpful in determination of electrode kinetics as per D_{Li^+}. Figure 4f−h shows the CV profiles of FeCoDA-CN@PP, FeSA-CN@PP, and CoSA-CN@PP separators, recorded at scan rates of 0.1, 0.2, 0.3, and 0.4 mV s^{-1}. The results show that the typical redox reaction capability of LSBs, with peak anode current (I_A) and peak cathode current (I_{C1}) (I_{C2}), is linearly related to the square root of the scan rate. To study the lithium-ion diffusion, the following classical Randles−Sevcik equation is employed

$$I_p = 2.65 \times 10^5 n^{1.5} S D_{Li^+} 0.5 \Delta C_{Li} \nu^{0.5} \quad (3)$$

where I_p denotes the peak current in CV measurements, S tells about the geometric area of the active electrode, n represents the electron transfer number, ν indicates the potential scan rate, D_{Li^+} gives lithium-ion diffusion efficiency, and C_{Li} determines the lithium ions concentration in the cathode. As S, n, and C_{Li} remain constant, the curve slope ($I_p/\nu^{0.5}$) becomes a function of the diffusion rate of lithium ions. As per the obtained results of D_{Li^+} for different modified separators, the lithium-ion diffusion rate is enhanced up to some extent. The two-atom synergistic catalysis of FeCoDA-CN-modified separators, whose own porous structure offers abundant active sites, is more favorable to boost the redox reaction in polysulfides. Hence, the rate of lithium-ion diffusion is fastest in A and C1 peaks (Figure 4i).

EIS of all of the prepared separators is performed at open circuit voltage (Figure S15). All of the Nyquist curves follow semicircle trends in the high-frequency range and diagonal line patterns in the low-frequency range, which can be credited to mass diffusion and charge transfer resistance (R_{ct}). After fitting the EIS results using Zview software (Figure S16), the R_{ct} of the PP separator is found to be 84.26 Ω. Its value is determined as 15.50, 27.71, and 37.45 Ω, for FeCoDA-CN@PP, FeSA-CN@PP, and CoSA-CN@PP separators, respectively. The results show that the modified membranes can offer faster Li^+ diffusion and effective redox conversion of polysulfides in LSBs, which is consistent with other obtained results.

LSBs assembled with the FeCoDA-CN@PP separator show an exceptional initial discharge capacity of 1404 mAh g^{-1} at 0.1C (1C = 1675 mAh g^{-1}; Figure 5a). It also delivers the highest reversible capacity of 1178 mAh g^{-1} at 0.1C. Also, it gives reversible capacities of 1165, 907, 792, and 652 mAh g^{-1}, respectively, at 0.2, 0.5, 1, and 2C, whereas the LSBs with CoSA-CN@PP, FeSA-CN@PP, and unmodified PP separators deliver reversible capacities of 1016, 868, and 721 mAh g^{-1} at 0.1C, respectively. These results indicate that the Fe and Co single-atom-doped nitrogen-rich carbon materials offer notable adsorption and catalytic conversion kinetics for polysulfides, but their specific discharge capacity at higher current density is not as high as that of the Fe and Co bimetallic single-atom system. This notable performance of LSBs with modified separators is attributed to the effectual inhibition of the LiPS shuttle effect and a fast ion/electron diffusion rate.

Figure 5b shows the comparison between positive potential peaks obtained during the first constant-current discharge plateau of LSBs with different separators. The battery with the FeCoDA-CN@PP separator gives the lowest polarization voltage and the battery with PP separators delivers the highest polarization voltage. This voltage difference is associated with the conversion of insoluble Li_2S to soluble LiPSs. The lower voltage difference proves that the reaction process is faster, which can be ascribed to the Fe and Co bimetallic single-atom catalytic system.

The charge/discharge response of LSBs with different separators measured at different rates is shown in Figures 5c and S17a−c. LSBs with the FeCoDA-CN@PP separator deliver a pronounced discharge platform, even at a rate of 2C, which indicates faster reaction kinetics. However, the LSBs with the pure PP separator have no discharge platform at a rate of 2C and the capacity decreases sharply. This can be due to the fact that LiPSs could not be quickly converted into polysulfides and could not reach the lithium negative electrode through the separator. The overpotentials of the charge/discharge platforms of LSBs with four different separators are compared in Figure 5d. The LSB with the FeCoDA-CN@PP separator shows the lowest overpotential, which is ascribed to the synergistic catalytic influence of the Fe and Co bimetallic single-atom system.

The FeCoDA-CN@PP separator consists of a two-atom synergistic catalytic system, which can enhance the cycling stability of LSBs by increasing the reaction kinetics and improving the sulfur utilization. The LSBs with the FeCoDA-CN@PP separator retain the highest discharge capacity of 963 mAh g^{-1} after 100 cycles provided at 0.2C along with a Coulombic efficiency of >95% (Figure 5e); this indicates the long cycling capacity of the cell. The cells with FeSA-CN@PP and CoSA-CN@PP separators show discharge capacities of 636 and 639 mAh g^{-1} after 100 cycles, respectively, whereas the PP separator showed a short-circuit overcharge phenomenon during the cycling. The FeCoDA-CN@PP separator can still retain a discharge capacity of 704 mAh g^{-1} after 200 cycles at 0.5C, as shown in Figure S18, whereas the FeSA-CN@PP and CoSA-CN@PP separators maintain discharge capacities of 607 and 497 mAh g^{-1} after 200 cycles, respectively. Moreover, the PP separator retains a discharge capacity of 385 mAh g^{-1} after 200 cycles.

To further investigate the cycling life of LSBs, the charge/discharge cycles are provided at a rate of 1C (Figure 5f). The battery with the FeCoDA-CN@PP separator still gives a discharge capacity of 541 mAh g^{-1}, and a higher and stable Coulombic efficiency of >95% after 500 cycles. These results give a capacity retention rate of 56%. The decay rate of average capacity is found to be 0.08% per cycle. The batteries with FeSA-CN@PP, CoSA-CN@PP, and PP separators deliver respective discharge capacities of 399, 477, and 230 mAh g^{-1}. The LSBs based on FeCoDA-CN@PP separators exhibit excellent electrochemical performance at 0.2 and 0.5C as well as 1C owing to the two-atom synergistic catalytic system, which can progress the consumption of active material sulfur and boost polysulfide conversion kinetics.

https://doi.org/10.1021/acsaem.2c04118
ACS Appl. Energy Mater. 2023, 6, 4671−4682

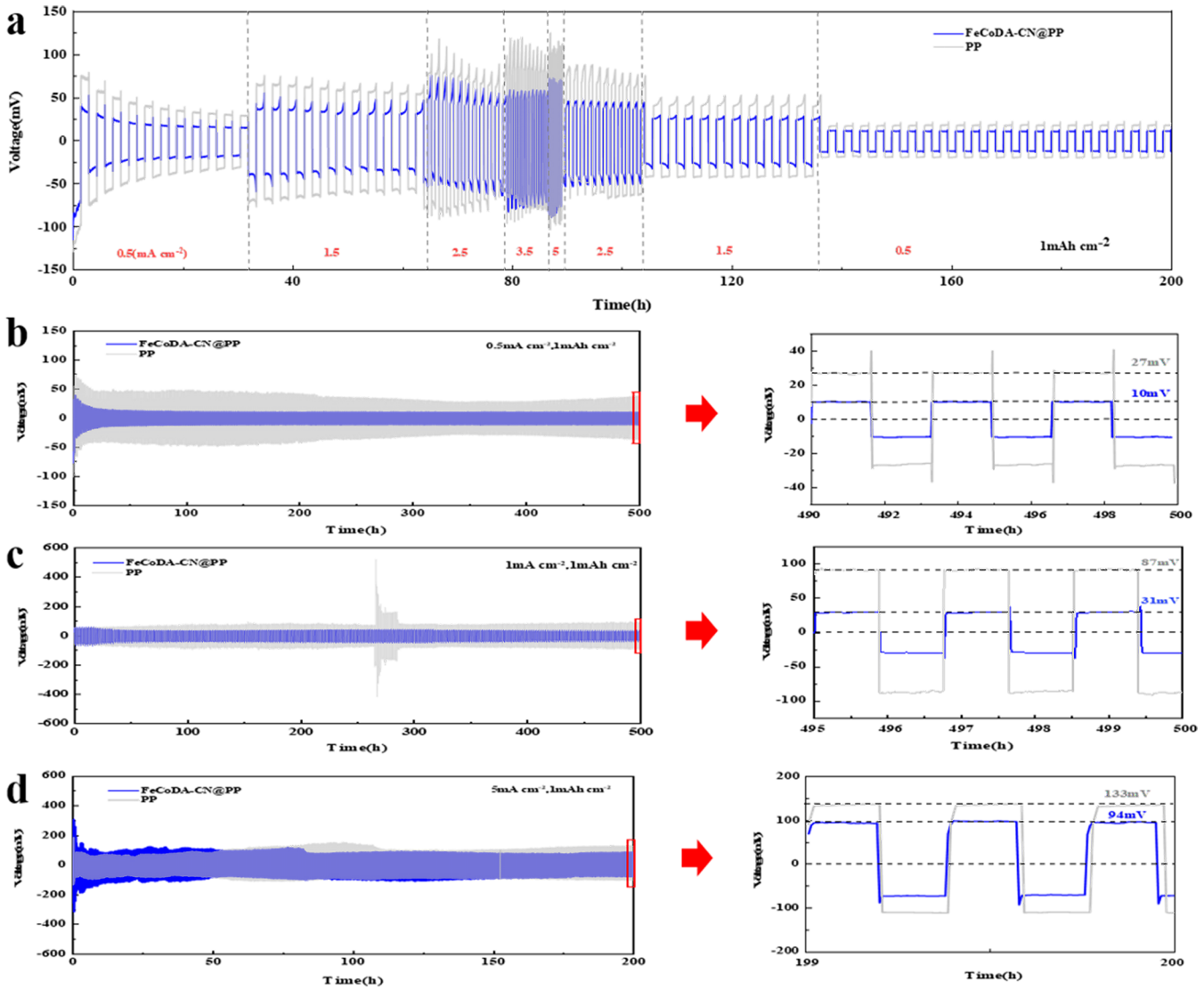

Figure 6. Assessment of cycling life of LSBs. (a) Rate evaluation of symmetric cells with PP and FeCoDA-CN@PP separators at a stripping/plating capacity of 1 mAh cm^{-2}. Voltage curves of Li||Li symmetric cells containing PP and FeCoDA-CN@PP separators, recorded at (b) 0.5 mA cm^{-2}, (c) 1 mA cm^{-2}, and (d) 5 mA cm^{-2} with a stripping/plating capacity of 1 mAh cm^{-2}.

To inspect the effect of the FeCoDA-CN@PP separator on the lithium metal anode, we assemble Li||Li symmetric cells with PP and FeCoDA-CN@PP separators and test their cycling stability at constant current. For stepwise provided current density from 0.5 to 5 mA cm^{-2} and then back to 0.5 mA cm^{-2}, the symmetric cell with the FeCoDA-CN@PP separator exhibits relatively small polarization against the PP separator (Figure 6a), which indicates its better multiplicity performance. The initial polarization voltage of a PP separator-based symmetric cell is measured as 76 mV at a current density of 0.5 mA cm^{-2}, which is about two times greater than that of a FeCoDA-CN@PP separator-based symmetric cell (36 mV), as depicted in Figure 6b. After 500 h of constant-current charge/discharge, the FeCoDA-CN@PP separator-based symmetric cell still maintains an overpotential as low as 10 mV. The polarization voltage of the PP separator-based cell suddenly increases to 500 mV at a current density of 1 mA cm^{-2} after 270 h of lithium coating/exfoliation (Figure 6c), which may be ascribed to lithium dendrites growth on the lithium metal anode surface. Such a situation leads to disintegration of the SEI layer and an increase in polarization voltage. Contrary to this, the FeCoDA-CN@PP separator-based symmetric cell maintains a stable voltage distribution and a low overpotential of 31 mV after 500 h. Figure 6d shows that even at a significantly high current density of 5 mA cm^{-2}, the FeCoDA-CN@PP separator-based symmetric cell maintains a polarization voltage of 94 mV and a relatively stable voltage distribution after 200 h of coating/exfoliation. These outcomes confirm that the diatomically doped nitrogen-rich carbon-coated modified separator plays crucial roles as a physical barrier and as a catalyst for uniform and enhanced lithium-ion flux. Consequently, the FeCoDA-CN@PP separator can promote uniform lithium plating/stripping and substantially enhance the lithium anode stability.

To study the inhibitory influence of the modified separator on the nucleation growth of lithium dendrites on the lithium anode surface, Li||Li symmetric cells with PP and FeCoDA-CN@PP separators are plated/peeled at a current density of 0.5 mA cm^{-2} (setting the plating/peeling capacity to 1 mAh cm^{-2}) for 500 h and then are disassembled to notice the evolution of lithium dendrites on the lithium anode surface. Figure S19 shows the SEM micrographs of the lithium metal

https://doi.org/10.1021/acsaem.2c04118
ACS Appl. Energy Mater. 2023, 6, 4671−4682

anode from a battery with the FeCoDA-CN@PP separator. The lithium surface does not show any obvious cracks, and no evidence is found of noticeable lithium dendrite growth, whereas in the case of the lithium metal anode from a battery with the PP separator, the cracking and pulverization on the lithium surface are obvious, and lithium dendrites and passivated dead lithium are observable at higher magnifications. These dendrites increase the polarization voltage in the battery. Thus, the long-term cycling stability of the Li||Li symmetric cell based on the FeCoDA-CN@PP separator is superior to the Li||Li symmetric cell with the PP separator. This outcome is consistent with other conducted investigations.

To further evaluate the performance of demonstrated separators for batteries with a diversity of electrode materials, PP and bimetallic single-atom-doped separators are used for the fabrication of LSBs with CNTs/S cathodes and lithium metal anodes. The batteries are provided with 300 cycles at a current density of 1C. Afterward, these are disassembled to observe the surface features of the lithium metal anode for lithium dendrite growth. The surface of the lithium metal anode from LSBs with the FeCoDA-CN@PP separator was relatively intact with no obvious dendrite growth or deposition of insoluble solid Li_2S (Figure 7a). This feature of the cell

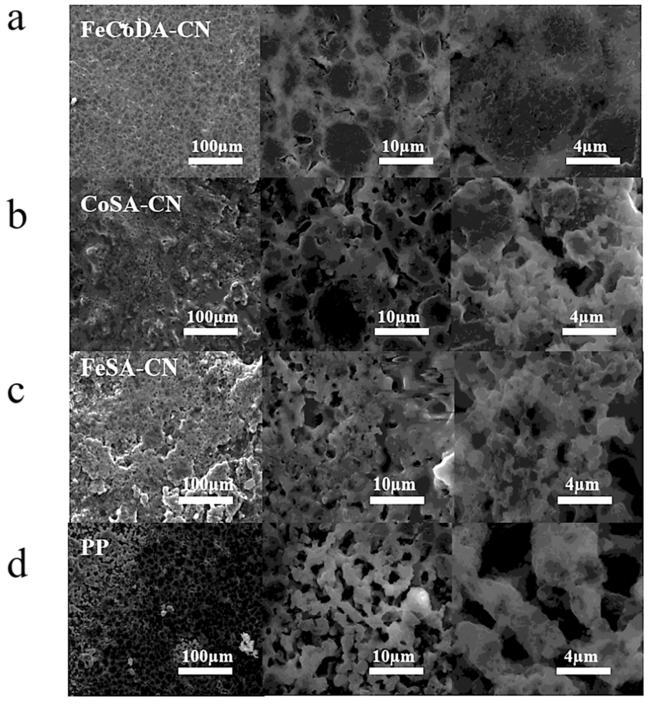

Figure 7. Analysis for direct observation of lithium dendrites. SEM images of the lithium metal anode from LSBs with (a) FeCoDA-CN@PP, (b) CoSA-CN@PP, (c) FeSA-CN@PP, and (d) PP separators after 300 charge/discharge cycles provided at 1C.

endows it with higher cycling performance and notable discharge specific capacity, and it exhibits excellent polysulfide shuttle inhibition and improves sulfur utilization.

The LSBs with CoSA-CN@PP and FeSA-CN@PP separators show formation of lithium dendrites and solid Li_2S growth on the Li metal anode surface after 300 cycles (Figure 7b,c). This drastically affects the specific capacity and cycling life of the cells. Moreover, the LSBs with the PP separator also show large dendritic growth and Li_2S deposition on the lithium metal anode, suggesting that the SEI film is completely destroyed (Figure 7d) during the working of the battery, which demolishes the specific capacity, cycling stability, and hence overall performance of the cell.

Figure S21 shows the XPS spectra after LiPS adsorption. The high-resolution C 1s spectrum shows that a new C−F peak is detected at 293.1 eV, which is highly correlated with the chemical bonding between FeCoDA-CN and LiPS. The strong chemical interaction may shift the electrons in the C atom toward the positron in LiPS; thus, all of the corresponding C═C (284.4 eV), C−N (285.2 eV), and O−C═O (288.5 eV) bonds are shifted to higher binding energies of 284.8, 286.7, and 290.1 eV, respectively, after cycling. N 1s spectra show that the peak intensity changed considerably. The sharp increase in the peak signal of pyrrole N should be attributed to the enhanced chemical interactions between FeCoDA-CN and S. FeCoDA-CN binds Co and Fe sites to balance the electron cloud density and exhibits different properties. Both Co $2p_{1/2}$ and Co $2p_{3/2}$ peaks shift to lower binding energy, same as Fe $2p_{3/2}$, while Fe $2p_{1/2}$ shifts to higher binding energy. The combination of Li and N is stronger, and the combination of the metal and S is also enhanced, indicating that FeCoDA-CN has a better double anchoring ability for LiPS. The proper adsorption ability through Li−N and M−S bonds hinders the diffusion of polysulfides, thus FeCoDA-CN cells have significant capacity retention.

The electrochemical response of all four separators evidences that LSBs with the FeCoDA-CN separator offer the best electrochemical performance in versatile conditions with a diversity of electrode materials owing to the synergistic influence of Fe and Co bimetallic doping. A comparison has been made between this conducted work and all other valuable published reports on LSBs based on MOF diaphragms, as given in Table S2. The demonstrated work has extensive advantages in terms of rate performance, specific capacity, cycle life, and overall performance of LSBs with modified layers.

4. CONCLUSIONS

The shuttling effect of polysulfides on the cathode and uncontrollable dendritic growth on the anode in LSBs are two major problems that affect the practical applications of these batteries. Here, we employed a three-dimensional dodecahedral material ZIF-8 as a coating on a multifunctional separator to boost its efficiency. The coating does not block the Li^+ transmission path on the PP separator. Owing to its porous structure, notable surface area, and high interfacial electronic conductivity, carbonized ZIF-8 provides an efficient and fruitful platform for designing the PP separator. Moreover, the synergistic catalysis effect of Fe and Co diatomic doping in the FeCoDA-CN@PP separator minimizes the shuttle effect of lithium polysulfides and ensures rapid ion/electron diffusion on the cathode. This favors the uniform lithium growth on the anode during the cycling of the battery. The LSBs assembled with the FeCoDA-CN@PP separator provide an initial discharge specific capacity of 1404 mAh g^{-1} at 0.1C. This discharge specific capacity is sustained up to 541 mAh g^{-1} after 500 cycles provided at 1C, which shows a capacity decay rate of just 0.08% per cycle. Moreover, the battery delivers a stable Coulombic efficiency of more than 95%. At a discharge density of 1 mA cm^{-2} with a plating/stripping capacity of 1 mAh cm^{-2}, the Li||Li symmetric cell with the FeCoDA-CN@PP separator

https://doi.org/10.1021/acsaem.2c04118
ACS Appl. Energy Mater. 2023, 6, 4671−4682

maintains a stable voltage distribution with an overpotential of 31 mV after 500 h. No obvious lithium dendrites are found on the anode surface after cycling, neither in the Li||Li symmetric cell nor the lithium−sulfur cell with the FeCoDA-CN@PP separator. The conducted research offers a feasible and upgraded method for the development of LSBs with higher capacity and longer life and encourages bimetallic atom catalysts for their uses in fabrication of high-energy-density storage devices.

■ ASSOCIATED CONTENT

Supporting Information

The Supporting Information is available free of charge at https://pubs.acs.org/doi/10.1021/acsaem.2c04118.

Additional SEM images; contact angle images; stress−stain curves; XPS spectra; BET pattern; CV curves; lithium-ion transference number images; EIS curves; equivalent circuit; charge/discharge curves; and long-term cycling performance (PDF)

■ AUTHOR INFORMATION

Corresponding Authors

Cunguo Wang − *Key Laboratory of Rubber-Plastics, Ministry of Education, Qingdao University of Science and Technology, Qingdao, Shandong 261500, China*; Email: wangcg@qust.edu.cn

Qi Li − *Key Laboratory of Nanodevices and Applications & Collaborative Innovation Center of Suzhou Nano Science and Technology, Suzhou Institute of Nano-Tech and Nano-Bionics, Chinese Academy of Sciences (CAS), Suzhou 215123, China*; orcid.org/0000-0002-0548-461X; Email: qli2013@sinano.ac.cn

Authors

Penghao Song − *Key Laboratory of Rubber-Plastics, Ministry of Education, Qingdao University of Science and Technology, Qingdao, Shandong 261500, China*

Surong Zheng − *Key Laboratory of Nanodevices and Applications & Collaborative Innovation Center of Suzhou Nano Science and Technology, Suzhou Institute of Nano-Tech and Nano-Bionics, Chinese Academy of Sciences (CAS), Suzhou 215123, China*

Zaka Ullah − *Department of Physics, Division of Science and Technology, University of Education, Lahore 54770, Pakistan*; orcid.org/0000-0002-2321-8323

Zairui Yang − *Key Laboratory of Nanodevices and Applications & Collaborative Innovation Center of Suzhou Nano Science and Technology, Suzhou Institute of Nano-Tech and Nano-Bionics, Chinese Academy of Sciences (CAS), Suzhou 215123, China*

Penghao Zhu − *Key Laboratory of Rubber-Plastics, Ministry of Education, Qingdao University of Science and Technology, Qingdao, Shandong 261500, China*

Aihua He − *Key Laboratory of Rubber-Plastics, Ministry of Education, Qingdao University of Science and Technology, Qingdao, Shandong 261500, China*

Complete contact information is available at: https://pubs.acs.org/10.1021/acsaem.2c04118

Author Contributions

‖P.S. and S.Z. contributed equally to this work.

Notes

The authors declare no competing financial interest.

■ ACKNOWLEDGMENTS

This work was supported by the National Natural Science Foundation of China (Grant No. 51972330), the Military Commission Logistics Department (Grant No. BY117J013), the State Key Program of the National Natural Science Foundation of China (Grant No. 61734008), the Natural Science Foundation of Jiangsu Province (Grant No. BK20210129), and the National Key Research and Development Program of China (2022YFB3704700(2022YFB3704702)) and the Taishan Scholar Program. The authors are grateful to Platforms of Characterization & Test, Collaborative Innovation Center of Suzhou Nano Science and Technology, and Nanofabrication Facility from Suzhou Institute of Nano-Tech and Nano-Bionics for their technical support and provision of experimental facilities.

■ REFERENCES

(1) Etacheri, V.; Marom, R.; Elazari, R.; Salitra, G.; Aurbach, D. Challenges in the development of advanced Li-ion batteries: a review. *Energy Environ. Sci.* **2011**, *4*, 3243−3262.

(2) Li, M.; Lu, J.; Chen, Z. W.; Amine, K. 30 years of Lithium-ion batteries. *Adv. Mater.* **2018**, *30*, No. 1800561.

(3) Manthiram, A.; Fu, Y. Z.; Su, Y. S. Challenges and prospects of Lithium-sulfur batteries. *Acc. Chem. Res.* **2013**, *46*, 1125−1134.

(4) Yin, Y. X.; Xin, S.; Guo, Y. G.; Wan, L. J. Lithium-sulfur batteries: electrochemistry, materials, and prospects. *Angew. Chem., Int. Ed.* **2013**, *52*, 13186−13200.

(5) Manthiram, A.; Chung, S. H.; Zu, C. X. Lithium-sulfur batteries: progress and prospects. *Adv. Mater.* **2015**, *27*, 1980−2006.

(6) Huang, Y. Z.; Lin, L.; Zhang, C. G.; Liu, L.; Li, Y. K.; Qiao, Z. S.; Lin, J.; Wei, Q. L.; Wang, L. S.; Xie, Q. S.; Peng, D. L. Recent advances and strategies toward polysulfides shuttle inhibition for high-performance Li-S batteries. *Adv. Sci.* **2022**, No. 2106004.

(7) Yang, S.; Zhang, J. F.; Tan, T. Z.; Zhao, Y.; Liu, N.; Li, H. P. A 3D MoS2/graphene microsphere coated separator for excellent performance Li-S batteries. *Materials* **2018**, *11*, No. 2064.

(8) Peng, H.-J.; Huang, J.-Q.; Cheng, X. B.; Zhang, Q. Review on high-loading and high-energy Lithium-sulfur batteries. *Adv. Energy Mater.* **2017**, *7*, No. 1700260.

(9) Bai, S. Y.; Liu, X. Z.; Zhu, K.; et al. Metal−organic framework-based separator for Lithium-sulfur batteries. *Nat. Energy* **2016**, *1*, No. 16094.

(10) Zhou, T. H.; Lv, W.; Li, J.; Zhou, G. M.; Zhao, Y.; Fan, S. X.; Liu, B. L.; Li, B. H.; Kang, F. Y.; Yang, Q. H. Twinborn TiO2-TiN heterostructures enabling smooth trapping-diffusion-conversion of polysulfides towards ultralong life Lithium-sulfur batteries. *Energy Environ. Sci.* **2017**, *10*, 1694−1703.

(11) Zhang, H. Y.; Xin, S. S.; Li, J.; Cui, H. T.; Liu, Y. Y.; Yang, Y. Z.; Wang, M. R. Synergistic regulation of polysulfides immobilization and conversion by MOF-derived CoP-HNC nanocages for high-performance Lithium-sulfur batteries. *Nano Energy* **2021**, *85*, No. 106011.

(12) Amine, R.; Liu, J. Z.; Acznik, I.; Sheng, T.; Lota, K.; Sun, H.; Sun, C. J.; Fic, K.; Zuo, X. B.; Ren, Y.; EI-Hady, D. A.; Alshitari, W.; AI-Bogami, A.; Chen, Z. H.; Amine, K.; Xu, G. L. Regulating the hidden solvation-ion-exchange in concentrated electrolytes for stable and safe lithium metal batteries. *Adv. Energy Mater.* **2020**, *10*, No. 2000901.

(13) Suo, L.; Hu, Y. S.; Li, H.; et al. A new class of Solvent-in-salt electrolyte for high-energy rechargeable metallic lithium batteries. *Nat. Commun.* **2013**, *4*, No. 1481.

(14) Chen, S. R.; Dai, F.; Gordin, M. L.; Yu, Z. X.; Gao, Y.; Song, J. X.; Wang, D. H. Functional organosulfide electrolyte promotes an

alternate reaction pathway to achieve high performance in Lithium-sulfur batteries. *Angew. Chem., Int. Ed.* **2016**, *55*, 4231−4235.
(15) Yang, T. Z.; Qian, T.; Liu, J.; Xu, N.; Li, Y. T.; Grundish, N.; Yan, C. L.; Goodenough, J. B. A new type of electrolyte system to suppress polysulfide dissolution for Lithium-sulfur battery. *ACS Nano* **2019**, *13*, 9067−9073.
(16) Ghazi, Z. A.; He, X.; Khattak, A. M.; Khan, N.; et al. MoS2/Celgard separator as efficient polysulfide barrier for long-life Lithium-sulfur batteries. *Adv. Mater.* **2017**, *29*, No. 1606817.
(17) Peng, H. J.; Wang, D. W.; Huang, J. Q.; Cheng, X. B.; Yuan, Z.; Wei, F.; Zhang, Q. Janus separator of polypropylene-supported cellular graphene framework for sulfur cathodes with high utilization in Lithium-sulfur batteries. *Adv. Sci.* **2016**, *3*, No. 1500268.
(18) Hou, T. Z.; Chen, X.; Peng, H. J.; Huang, J. Q.; Li, B. Q.; Zhang, Q.; Li, B. Design principles for heteroatom-doped nanocarbon to achieve strong anchoring of polysulfides for Lithium-sulfur batteries. *Small* **2016**, *12*, 3283−3291.
(19) Balach, J.; Jaumann, T.; Klose, M.; Oswald, S.; Eckert, J.; Giebeler, L. Improved cycling stability of Lithium−sulfur batteries using a polypropylene-supported nitrogen-doped mesoporous carbon hybrid separator as polysulfide adsorbent. *J. Power Sources* **2016**, *303*, 317−324.
(20) Ai, W.; Zhou, W. W.; Du, Z. Z.; Chen, Y.; Sun, Z. P.; et al. Nitrogen and phosphorus co-doped hierarchically porous carbon as an efficient sulfur host for Li-S batteries. *Energy Storage Mater.* **2017**, *6*, 112−118.
(21) Gu, X.; Tong, C.-j.; Lai, C.; Qiu, J.; Huang, X.; Yang, W.; Wen, B.; Liu, L.-m.; Hou, Y.; Zhang, S. A porous nitrogen and phosphorous dual doped graphene blocking layer for high performance Li−S batteries. *J. Mater. Chem. A* **2015**, *3*, 16670−16678.
(22) Pan, H. Y.; Tan, Z.; Zhou, H. H.; Jiang, L. L.; Huang, Z. Y.; Feng, Q. X.; Zhou, Q.; Ma, S.; Kuang, Y. F. Fe3C-N-doped carbon modified separator for high performance Lithium-sulfur batteries. *Energy Chem.* **2019**, *39*, 101−108.
(23) Jin, Z. Q.; Xie, K.; Hong, X. B.; Hu, Z. Q.; Liu, X. Application of lithiated Nafion ionomer film as functional separator for Lithium-sulfur cells. *J. Power Sources* **2012**, *218*, 163−167.
(24) Yu, X. W.; Wu, H.; Koo, J. H.; Manthiram, A. Tailoring the pore size of a polypropylene separator with a polymer having intrinsic nanoporosity for suppressing the polysulfide shuttle in Lithium−sulfur batteries. *Adv. Energy Mater.* **2019**, *10*, No. 1902872.
(25) Tsao, Y. C.; Gong, H. X.; Chen, S. C.; Chen, G.; Liu, Y. Z.; Gao, T. Z.; Cui, Y.; Bao, Z. A nickel-decorated carbon flower/sulfur cathode for lean-electrolyte Lithium-sulfur batteries. *Adv. Energy Mater.* **2021**, *11*, No. 2101449.
(26) Liu, Y. N.; Wei, Z. Y.; Zhong, B.; Wang, H. T.; Xia, L.; Zhang, T.; Duan, X. M.; Jia, D. C.; Zhou, Y.; Huang, X. X. O-, N-Coordinated single Mn atoms accelerating polysulfides transformation in Lithium-sulfur batteries. *Energy Storage Mater.* **2021**, *35*, 12−18.
(27) Zhang, L. L.; Liu, D. B.; Muhammad, Z.; Wan, F.; Xie, W.; Wang, Y. J.; Song, L.; Niu, Z. Q.; Chen, J. Single nickel atoms on nitrogen-doped graphene enabling enhanced kinetics of Lithium-sulfur batteries. *Adv. Mater.* **2019**, *31*, No. 1903955.
(28) Wang, C. G.; Song, H. W.; Yu, C. C.; Ullah, Z.; Guan, Z. X.; Chu, R. R.; Zhang, Y. F.; Zhao, L. Y.; Li, Q.; Liu, L. W. Iron single-atom catalyst anchored on nitrogen-rich MOF-derived carbon nanocage to accelerate polysulfide redox conversion for Lithium-sulfur batteries. *J. Mater. Chem. A* **2020**, *8*, 3421−3430.
(29) Lin, Z.; Li, X.; Huang, W.; et al. Active platinum nanoparticles as a bifunctional promoter for Lithium-sulfur batteries. *ChemElectroChem* **2017**, *4*, 2577−2582.
(30) Li, Y. J.; Zhou, P.; Li, H.; Gao, T. T.; Zhou, L.; Zhang, Y. L.; Xiao, N.; Xia, Z. H.; Wang, L.; Zhang, Q. H.; Gu, L.; Guo, S. J. A freestanding flexible single-atom cobalt-based multifunctional interlayer toward reversible and durable Lithium-sulfur batteries. *Small Methods* **2020**, *4*, No. 1900701.
(31) Wang, J.; Jia, L. J.; Zhong, J.; Xiao, Q. B.; Wang, C.; Zang, K. T.; Liu, H. T.; Zheng, H. C.; Luo, J.; Yang, J.; Fan, H. Y.; Duan, W. H.; Wu, Y.; Lin, H. Z.; Zhang, Y. G. Single-atom catalyst boosts electrochemical conversion reactions in batteries. *Energy Storage Mater.* **2019**, *18*, 246−252.
(32) Wang, J.; Jia, L. J.; Duan, S. R.; Liu, H.; Xiao, Q. B.; Li, T.; Fan, H. Y.; Feng, K.; Yang, J.; Wang, Q.; Liu, M. N.; Zhong, J.; Duan, W. H.; Lin, H. Z.; Zhang, Y. G. Single atomic cobalt catalyst significantly accelerates lithium-ion diffusion in high mass loading Li2S cathode. *Energy Storage Mater.* **2020**, *28*, 375−382.
(33) Zhang, K.; Chen, Z. X.; Ning, R. Q.; Xi, S. B.; Tang, W.; Du, Y. H.; Liu, C. B.; Ren, Z. Y.; Chi, X.; Bai, M. H.; Shen, C.; Li, X.; Wang, X. W.; Zhao, X. X.; Leng, K.; Pennycook, S. J.; Li, H. P.; Xu, H.; Loh, K. P.; Xie, K. Y. Single-atom coated separator for robust Lithium-sulfur batteries. *ACS Appl. Mater. Interfaces* **2019**, *11*, 25147−25154.
(34) Chen, Y.; Kang, Y. H.; Yang, H. Y.; Hua, H. M.; Qin, J. X.; Liu, P.; Zhang, Y. Y.; Zhang, Y. J.; Zhao, J. B. Contribution of different metal nodes on stepwise electrocatalysis in lithium-sulfur batteries. *Energy Storage Mater.* **2023**, *54*, 488−497.

https://doi.org/10.1021/acsaem.2c04118
ACS Appl. Energy Mater. 2023, 6, 4671−4682